

1 Detection of slow slip events using wavelet
2 analysis of GNSS recordings

3 Ariane Ducellier¹, Kenneth C. Creager², and David A. Schmidt²

4 ¹Corresponding author. University of Washington, Department of
5 Earth and Space Sciences, Box 351310, 4000 15th Avenue NE
6 Seattle, WA 98195-1310

7 ²University of Washington, Department of Earth and Space
8 Sciences

9 **Key points**

- 10 • We use a wavelet-based signal processing method to detect transients in
11 GNSS data, such as slow slip events.
- 12 • There is a good correlation between detections of slow slip using GNSS
13 data and using tremor data.
- 14 • The method could be applied in regions where no tremor is detected in
15 conjunction with slow slip events.

₁₆ **Abstract**

₁₇ In many places, tectonic tremor is observed in relation to slow slip and can
₁₈ be used as a proxy to study slow slip events of moderate magnitude where
₁₉ surface deformation is hidden in Global Navigation Satellite System (GNSS)
₂₀ noise. However, in subduction zones where no clear relationship between tremor
₂₁ and slow slip occurrence is observed, these methods cannot be applied, and we
₂₂ need other methods to be able to better detect and quantify slow slip. Wavelets
₂₃ methods such as the Discrete Wavelet Transform (DWT) and the Maximal
₂₄ Overlap Discrete Wavelet Transform (MODWT) are mathematical tools for
₂₅ analyzing time series simultaneously in the time and the frequency domain by
₂₆ observing how weighted differences of a time series vary from one period to the
₂₇ next. In this paper, we use wavelet methods to analyze GNSS time series and
₂₈ seismic recordings of slow slip events in Cascadia. We use detrended GNSS
₂₉ data, apply the MODWT transform and stack the wavelet details over several
₃₀ nearby GNSS stations. As an independent check on the timing of slow slip
₃₁ events, we also compute the cumulative number of tremor in the vicinity of the
₃₂ GNSS stations, detrend this signal, and apply the MODWT transform. In both
₃₃ time series, we can then see simultaneous waveforms whose timing corresponds
₃₄ to the timing of slow slip events. We assume that there is a slow slip event
₃₅ whenever there is a positive peak followed by a negative peak in the wavelet
₃₆ signal. We verify that there is a good correlation between slow slip events
₃₇ detected with only GNSS data, and slow slip events detected with only tremor
₃₈ data for northern Cascadia. The wavelet-based detection method detects well
₃₉ events of magnitude higher than 6 as determined by independent event catalogs
₄₀ (e.g. [Michel et al., 2019]).

41 **1 Introduction**

42 Slow slip events are a new feature discovered in the last two decades in many
43 subduction zones thanks to recordings of the displacement of Earth's surface by
44 dense Global Navigation Satellite System (GNSS) networks [Vergnolle et al.,
45 2010, Schmidt and Gao, 2010, Jiang et al., 2012, Wallace et al., 2012].
46 As with ordinary earthquakes, slow slip events represent slip on a fault, for in-
47 stance the plate boundary between a tectonic plate subducting under another
48 tectonic plate. However, they take a much longer time (several days to several
49 years) to happen relative to ordinary earthquakes. They have a relatively short
50 recurrence time (months to years) compared to the recurrence time of regular
51 earthquakes (up to several hundreds of years), allowing scientists to observe
52 and study many complete event cycles, which is typically not possible to ex-
53 plore with traditional earthquake catalogs [Beroza and Ide, 2011]. A slow slip
54 event on the plate boundary is inferred to happen when there is a reversal of
55 the direction of motion at GNSS stations, compared to the secular interseismic
56 motion. Slow slip events have been observed in many places [Beroza and
57 Ide, 2011, Audet and Kim, 2016], such as Cascadia [Bartlow, 2020],
58 Nankai [Nishimura et al., 2013], Alaska [Li et al., 2016], Costa Rica
59 [Jiang et al., 2012], Mexico [Radiguet et al., 2012], and New Zealand
60 [Wallace, 2020].

61

62 In many places, tectonic tremor is also observed in relation to slow slip, but
63 it is more abundant in some places [Hall et al., 2018]. Tremor is a long
64 (several seconds to many minutes), low amplitude seismic signal, with emergent
65 onsets, and an absence of clear impulsive phases. Tectonic tremor have been
66 explained as a swarm of small, low-frequency earthquakes (LFEs) [Shelly et al.,
67 2007], which are small magnitude earthquakes ($M \sim 1$) for which frequency

content (1-10 Hz) is lower than for ordinary earthquakes (up to 20 Hz). In subduction zones such as Nankai and Cascadia, tectonic tremor observations are spatially and temporally correlated with slow slip observations [Obara, 2002, Rogers and Dragert, 2003]. Due to this correlation, these paired phenomena have been called Episodic Tremor and Slip (ETS). However, this is not always the case. For instance, in northern New Zealand, tremor is more challenging to detect, and seems to be located downdip of the slow slip on the plate boundary [Todd and Schwartz, 2016]. In Alaska, the tremor zone only partially overlaps the long-term slow slip zone and there does not appear to be any temporal correlation between tremor and slow slip occurrence [Wech, 2016].

78

In Cascadia, there are robust signals in both GNSS and tremor [**Hawthorne and Rubin, 2013**]. This is also the case in Nankai [**Hiramatsu et al., 2008**], where tiltmeters are used instead of GNSS. It is thus possible to use tremor as a proxy to observe slow slip events that are not directly observed in the GNSS data. For instance, Aguiar et al. [2009] studied 23 ETS events in Cascadia with more than 50 hours of tectonic tremor. For all these events, they computed both the GPS-estimated moment release and the cumulative number of hours of tectonic tremor recorded. They observed a linear relationship between moment release and number of hours of tremor for ETS events of moment magnitude 6.3 to 6.8. Based on this linear relationship, it is possible to infer the existence of smaller slow slip events of magnitude 5-6 occurring simultaneously with smaller tremor bursts of duration 1 to 50 hours occurring in between the big ETS events, and for which there is no detectable signal in the GPS data.

92

Frank [2016] divided GPS time series observations from Cascadia and Guerrero, Mexico, into two groups: the first group contains days with abundant

95 tremor and LFEs, the second group contains days when the number of tremor
96 or LFEs is lower than a threshold. He then stacked separately the two groups
97 of daily observations and observed a cumulative displacement in the direction
98 corresponding to the loading period when few tremor or LFEs are observed
99 and the surface deformation corresponds to the secular plate motion. He also
100 observed a cumulative displacement in the opposite direction corresponding to
101 the release period when tremor and LFEs are observed. He was thus able to
102 observe a reverse displacement corresponding to smaller slow slip events not
103 directly observable in the GPS data for individual events.

104

105 However, these methods cannot be applied to detect slow slip events in places
106 where tremor and slow slip occurrence are not well spatially and temporally cor-
107 related, tremor is not abundant, or the seismic network is not robust enough.
108 We thus need other methods to be able to better detect and quantify slow slip.

109

110 Wavelet methods such as the Discrete Wavelet Transform (DWT) are math-
111 ematical tools for analyzing time series simultaneously in the time and the fre-
112 quency domain by observing how weighted differences of a time series vary from
113 one period to the next. Wavelet methods have been widely used for geophysical
114 applications (e.g. Kumar and Foufoula-Georgiou [1997]). However, few studies
115 have used wavelet methods to analyze recordings of slow slip, and their scope
116 was limited to the detection of the bigger (magnitude 6-7) short-term (a few
117 weeks) events [Szeliga et al., 2008, Ohtani et al., 2010, Wei et al., 2012, Alba
118 et al., 2019].

119

120 Szeliga et al. [2008] determined the timing and the amplitude of 34 slow
121 slip events throughout the Cascadia subduction zone between 1997 and 2005

122 using wavelets. They modeled the GPS time series by the sum of a linear trend,
123 annual and biannual sinusoids representing seasonal effects, Heaviside step func-
124 tions corresponding to earthquakes and hardware upgrades, and a residual sig-
125 nal. They then applied a Gaussian wavelet transform to the residual time series
126 to get the exact timing of slow slip at each GPS station. The idea is that the
127 wavelet transform allows us to analyze the signal both in the time and the fre-
128 quency domains. A sharp change in the signal will be localized and seen at all
129 levels of the wavelet decomposition, contrary to what happens with the periodic
130 sinusoids of the Fourier transform.

131

132 Instead of using wavelets in the time domain, Ohtani et al. [2010] used 2D
133 wavelet functions in the spatial domain to detect slow slip events. They de-
134 signed the Network Stain Filter (NSF) to detect transient deformation signals
135 from large-scale geodetic arrays. They modeled the position of the GPS station
136 by the sum of the secular velocity, a spatially coherent field, site-specific noise,
137 reference frame errors, and observation errors. The spatial displacement field is
138 modeled by the sum of basis wavelets with time-varying weights. Their method
139 has been successfully used to detect a transient event in the Boso peninsula,
140 Japan, and a slow slip event in the Alaska subduction zone [Wei et al., 2012].

141

142 Finally, Alba et al. [2019] used hourly water level records from four tide
143 gauges in the Juan de Fuca Straight and the Puget Sound to determine rela-
144 tive vertical displacements associated with ETS events between 1996 and 2011.
145 Their main idea is that the tidal level measured at a given gauge is the sum of
146 a noise component at multiple timescales (tides, ocean and atmospheric noise)
147 and an uplift signal due to the ETS events. The noise component is assumed to
148 be coherent between all tidal gauges, while the tectonic uplift signal is different

149 provided that the gauges are far enough from each other. By stacking the tidal
150 records after removing tides, the uplift signals cancel each other while the noise
151 signal is amplified. By stacking the details of the DWT decomposition, instead
152 of stacking the raw tidal record, each of the components of the noise at different
153 time scales is retrieved and can then be removed from the raw records to obtain
154 the uplift signal. The authors were then able to clearly see a difference in uplift
155 between the two tidal gauges at Port Angeles and Port Townsend.

156

157 In our study, we use a similar approach to previous studies with a different
158 reasoning. We only stack signals at nearby GPS stations, assuming that the
159 longitudinal displacement due to the ETS events will then be the same at each
160 of the GPS stations considered. We suppose that some of the noise component
161 is different at each GPS station and will be eliminated by the stacking. Fi-
162 nally, we assume that the noise and the longitudinal displacement due to the
163 ETS events and the secular plate motion have different time scales, so that the
164 wavelet decomposition will act as a bandpass filter to retrieve the displacement
165 signal and highlight the ETS events. We use wavelet methods to analyze GPS
166 and tremor recordings of slow slip events in Cascadia. Our objective is to verify
167 that there is a good correlation between slow slip events detected with only
168 GNSS data, and slow slip events detected with only tremor data. We thus want
169 to demonstrate that the wavelet-based detection method can be applied to de-
170 tect slow slip events that may currently be obscured using standard methods.

171

172 2 Data

173 We focused our study on northwest Washington State. For the GNSS data, we
174 used the GPS time series provided by the Pacific Northwest Geodetic Array,

175 Central Washington University. These are network solutions **in ITRF2014**
176 **with phase ambiguities resolved with wide-lane phase-biases and or-**
177 **bits and satellite clocks provided by the Jet Propulsion Laboratory/NASA.**
178 North, East, and Vertical directions are available. However, as the direction of
179 the secular plate motion is close to the East direction, we only used the East
180 direction of the GPS time series for the data analysis, as it has the best signal-
181 to-noise ratio. The wavelet method works best with data with zero mean, and
182 no sharp discontinuities; so we use the cleaned dataset, that is GPS times series
183 with linear trends, steps due to earthquakes or hardware upgrades, and annual
184 and semi-annual sinusoids signals simultaneously estimated and removed follow-
185 ing Szeliga et al. [2004]. For the tremor data, we used the tremor catalog from
186 the Pacific Northwest Seismic Network (PNSN) [Wech, 2010].

187

188 3 Method

189 3.1 The Maximal Overlap Discrete Wavelet Transform

190 The Discrete Wavelet Transform (DWT) is an orthonormal transform that
191 transforms a time series X_t ($t = 0, \dots, N - 1$) into a vector of wavelet coeffi-
192 cients W_i ($i = 0, \dots, N - 1$). If we denote J the level of the wavelet decom-
193 position, and the number of observations is equal to $N = n * 2^J$, where **n is**
194 **some integer greater than or equal to 1**, the vector of wavelet coefficients
195 can be decomposed into J wavelet vectors W_j of lengths $\frac{N}{2}, \frac{N}{4}, \dots, \frac{N}{2^J}$, and
196 one scaling vector V_J of length $\frac{N}{2^J}$. Each wavelet vector W_j is associated with
197 changes on time scale $\tau_j = dt2^{j-1}$, where dt is the time step of the time se-
198 ries, and corresponds to the filtering of the original time series with a filter
199 with nominal frequency interval $[\frac{1}{dt2^{j+1}}; \frac{1}{dt2^j}]$. The scaling vector V_J is associ-

200 ated with averages in time scale $\lambda_J = dt2^J$, and corresponds to the filtering of
 201 the original time series with a filter with nominal frequency interval $[0; \frac{1}{dt2^{J+1}}]$.
 202 Wavelet vectors can be further decomposed into details and smooths, which are
 203 more easily interpretable. We define for $j = 1, \dots, J$ the j th wavelet detail
 204 D_j , which is a vector of length N , and is associated to time scale $\tau_j = dt2^{j-1}$.
 205 Similarly, we can define for $j = 1, \dots, J$ the j th wavelet smooth S_j , which is a
 206 vector of length N , and is associated to scales $\tau_{j+1} = dt2^{j+1}$ and higher. The
 207 basic idea is to reapply to W_j the wavelet filter that was used to construct W_j
 208 from the initial time series X . Together, the details and the smooths define the
 209 multiresolution analysis (MRA) of X :

$$210 \quad X = \sum_{j=1}^J D_j + S_J \quad (1)$$

211 The DWT presents several disadvantages. First, the length of the time se-
 212 ries must be a multiple of 2^J where J is the level of the DWT decomposition.
 213 Second, the time step of the wavelet vector W_j is $dt2^j$, which may not corre-
 214 spond to the time when some interesting phenomenon is visible on the original
 215 time series. Third, when we circularly shift the time series, the corresponding
 216 wavelet coefficients, details and smooths are not a circularly shifted version of
 217 the wavelet coefficients, details and smooths of the original time series. Thus,
 218 the values of the wavelet coefficients, details and smooths are strongly dependent
 219 on the time when we start experimentally gathering the data. Finally, when we
 220 filter the time series to obtain the details D_j and smooths S_j , we introduce a
 221 phase shift, which makes it difficult to line up meaningfully the features of the
 222 MRA with the original time series.

223

224 To overcome the disadvantages described above, we use instead the Maxi-
 225 mal Overlap Discrete Wavelet Transform (MODWT). The MODWT transforms

226 the time series X_t ($t = 0, \dots, N - 1$) into J wavelet vectors \tilde{W}_j ($j = 1, \dots, J$) of
 227 length N and a scaling vector \tilde{V}_J of length N . As is the case for the DWT,
 228 each wavelet vector \tilde{W}_j is associated with changes on scale $\tau_j = dt2^{j-1}$, and
 229 corresponds to the filtering of the original time series with a filter with nominal
 230 frequency interval $[\frac{1}{dt2^{j+1}}; \frac{1}{dt2^j}]$. The scaling vector \tilde{V}_J is associated with aver-
 231 ages in scale $\lambda_J = dt2^J$, and corresponds to the filtering of the original time
 232 series with a filter with nominal frequency interval $[0; \frac{1}{dt2^{J+1}}]$. As is the case for
 233 the DWT, we can write the MRA:

$$234 \quad X = \sum_{j=1}^J \tilde{D}_j + \tilde{S}_J \quad (2)$$

235 The MODWT of a time series can be defined for any length N . The time
 236 step of the wavelet vectors \tilde{W}_j and the scaling vector \tilde{V}_J is equal to the time
 237 step of the original time series. When we circularly shift the time series, the
 238 corresponding wavelet vectors, scaling vector, details and smooths are shifted
 239 by the same amount. The details and smooths are associated with a zero phase
 240 filter, making it easy to line up meaningfully the features of the MRA with the
 241 original time series. The wavelet methods for time series analysis are explained
 242 in a more detailed way in [Percival and Walden, 2000]).
 243

244 3.2 Application to synthetic data

245 To illustrate the wavelet transform method, we first apply the MODWT to syn-
 246 thetic data. As slow slip events occur in Cascadia on a regular basis, every
 247 twelve to eighteen months, we create a synthetic signal of period $T = 500$ days.
 248 To reproduce the ground displacement observed on the longitudinal component
 249 of GPS stations in Cascadia, we divide each period into two parts: In the first
 250 part of duration $T - N$, the displacement is linearly increasing and corresponds

251 to the inter seismic plate motion in the eastern direction; in the second part
252 of duration N , the displacement is linearly decreasing and corresponds to a
253 slow slip event on a reverse fault at depth triggering a ground displacement in
254 the western direction. To see the effect of the duration of the slow slip event,
255 we use different values for $N = 5, 10, 20, 40$ days. The amplitude of the set is
256 normalized to 1. Figure 1 shows the synthetics, the details D_j of the wavelet
257 decomposition for levels 1 to 10, and the smooth S_{10} for the four durations of a
258 slow slip event.

259

260 The ramp-like signal is transformed through the wavelet filtering into a wave-
261 form with first a positive peak and then a negative peak. The shape of the wave-
262 form is the same for every level of the wavelet decomposition, but the width of
263 the waveform increases with the scale level. For the 8th level of the wavelet de-
264 composition, the width of the waveform is nearly as large as the time between
265 two events. At larger scales, the waveforms start to merge two contiguous events
266 together, and make the wavelet decomposition less interpretable. For an event
267 of duration 5 days, the wavelet details at levels higher than 3 have a larger
268 amplitude than the wavelet details at lower scales. For an event of duration 10
269 days, the wavelet details at levels higher than 4 have a larger amplitude than
270 the wavelet details at lower scales. For an event of duration 20 days, the wavelet
271 details at levels higher than 5 have a larger amplitude than the wavelet details
272 at lower scales. For an event of duration 40 days, the wavelet details at levels
273 higher than 6 have a larger amplitude than the wavelet details at lower scales.
274 Thus, the scale levels at which an event is being seen in the wavelet details give
275 us an indication about the duration (and the magnitude) of the slow slip event.
276 The big slow slip events of magnitude 6-7 typically trigger a signal that lasts
277 about one week at an individual GPS station, and the whole event lasts several

278 weeks. We expect them to start being visible at the level 5 of the wavelet de-
279 composition, but to not be noticeable at lower time scales.

280

281 3.3 MODWT of GPS and tremor data

282 The DWT and MODWT methods must be used on a continuous time series,
283 without gaps in the recordings. To deal with the gaps in the GNSS recordings,
284 we simply replace the missing values by interpolation. The value for the first
285 day for which data are missing is equal to the mean of the five days before
286 the gap. The value for the last day for which data are missing is equal to the
287 mean of the five days after the gap. The remaining missing values are com-
288 puted by doing a linear interpolation of the first and the last values and adding
289 a Gaussian noise component with mean zero and standard deviation equal to
290 the standard deviation of the whole time series. The straight line starts at and
291 ends at . We verify how the wavelet details may be affected by looking at a GPS
292 time series without missing values and compared the wavelet details with and
293 without removing some data points. Station PGC5 recorded continuous 1390
294 days between 2009 and 2013 without any missing values. We first computed
295 the wavelet details without missing values. Then, we removed ten neighboring
296 values, replaced them using the method described above (linear interpolation
297 plus Gaussian noise), and computed the wavelet details with the replaced val-
298 ues. Figure 2 shows a comparison of the two wavelet details for two different
299 locations of the missing values. We can see that there are visible differences
300 in the time series itself, and in the details at the smallest levels of the wavelet
301 decomposition. However, the differences between the wavelet details with and
302 without missing values get smaller and smaller with increasing levels of details,
303 and are barely visible for the levels that are most relevant (levels 6 and above).

304 We thus conclude that we can easily replace the missing values in the GNSS
305 time series without introducing false detections of slow slip events.

306

307 We then applied the wavelet filtering to real GPS data. Figure 3 shows the
308 longitudinal displacement for GPS station PGC5, located in southern Vancou-
309 ver Island, the details of the wavelet decomposition for levels 1 to 8, and the
310 smooth. In the data, we can see a sharp drop in displacement whenever there is
311 a documented slow slip event. For levels 5 to 8, which correspond to time scales
312 16, 32, 64 and 128 days, we can see in the details a positive peak followed by
313 a negative peak whenever there is a drop in displacement in the data. We thus
314 verify that the wavelet method can detect steps in the time series associated
315 with slow slip events.

316

317 To increase the signal-to-noise ratio and better detect slow slip events, we
318 stack the signal from several neighboring GPS stations. We choose to focus on
319 GPS stations located close enough to the tremor zone to get a sufficiently high
320 amplitude of the slow slip signal. We choose 16 points along the 40 km depth
321 contour of the plate boundary (model from Preston et al. [2003]) with spacing
322 equal 0.1 degree in latitude (red triangles on Figure 4). Then we took all the
323 GPS stations located in a 50 km radius for a given point, compute the wavelet
324 details for the longitudinal displacement of each station, and stack each detail
325 over the GPS stations. We thus have a stacked detail for each level 1 to 10 of
326 the wavelet decomposition.

327

328 To assess the success of the wavelet decomposition for detecting slow slip
329 events in GPS time series, we validate the approach by comparing to an inde-
330 pendent proxy for ETS events. We took all the tremor epicenters located within

331 a 50 km radius centered on one of the 16 locations marked by red triangles on
332 Figure 3. Then we computed the cumulative number of tremor within this
333 circle. Finally, we removed a linear trend from the cumulative tremor count,
334 and applied the wavelet transform. Figure 5 shows an example of the wavelet
335 decomposition for the third northernmost location on Figure 4 (which is closest
336 to GPS station PGC5). Contrary to what happens for the GPS data, we see
337 a sharp increase in the time series whenever there is a tremor episode, which
338 translates into a negative peak followed by a positive peak in the wavelet details.

339 4 Results

340 We stacked the 8th level detail of the wavelet decomposition of the displacement
341 over all the GPS stations located in a 50 km radius of a given point, for the 16
342 locations indicated in Figure 3. The result is shown in the top panel of Figure 6,
343 where each line represents one of the locations along strike. To better highlight
344 the peaks in the wavelet details, we highlighted in red the time intervals where
345 the amplitude of the stacked detail is higher than a threshold, and in blue the
346 time intervals where the amplitude of the stacked detail is lower than minus the
347 threshold. To compare the GPS signal with the tremor signal, we plotted the
348 8th level detail of the wavelet decomposition of the tremor count on the bottom
349 panel of Figure 6. We multiplied by -1 the cumulative tremor count for the
350 wavelet decomposition in order to be able to match positive peaks with positive
351 peaks and negative peaks with negative peaks. In the tremor catalog from the
352 PNSN, there are 17 tremor events with more than 150 hours of tremor recorded.
353 The events are summarized in Table 1. The time of the event is the start date
354 plus half the duration of the event.

355

356 Although the latitudinal extension of the events is not always the same for

357 the GPS data and for the tremor data, we identify the same 13 events in both 8th
358 wavelet decompositions for the 8th level: January 2007, May 2008, May 2009,
359 August 2010, August 2011, September 2012, September 2013, August-November
360 2014, January 2016, March 2017, June 2018, March-November 2019, and Oc-
361 tober 2020-January 2021. Although there are two events in the tremor catalog
362 in August 2014 and November 2014, these two events are not distinguishable in
363 the 8th level details and look more like a single event slowly propagating from
364 South to North. The same phenomenon is observed in 2019 when two tremor
365 events in March and November 2019 are merged into a single event propagating
366 slowly from South to North. In 2020-2021, the wavelet decomposition of the
367 tremor shows one event in the south in October-November 2020 and one event
368 in the North in January 2021, but in the wavelet decomposition of the GPS
369 data, these three events look like a single event propagating slowly from South
370 to North.

371

372 A similar comparison is shown for the wavelet decomposition of the GPS
373 data and the wavelet decomposition of the tremor count data for the 7th level
374 and the 6th level respectively (Figures 7 and 8). The events are harder to see in
375 the 7th level than in the 8th level, both for the GPS data and the tremor count
376 data. The wavelet decomposition is more noisy for the GPS data between 2010
377 and 2012, but it does not seem that there are more slow slip events visible in
378 the 7th level.

379

380 For the 6th level detail, we see an additional event in the South in Fall 2009
381 that is present both in the GPS and the tremor data. It may correspond to the
382 northern extent of a big ETS event occurring in Fall 2009 south of the study
383 area (event 19 in the Michel et al. [2019] catalog). There are three small sig-

384 nals in the GPS data in Winter 2012, Fall 2017, and Winter 2020 that are not
385 present in the tremor data, and may be false detections. To summarize, we
386 assume that true detections are events present in both GPS and tremor time
387 series, and false detections are events present in the GPS but not in the tremor
388 time series. Then, all the 13 events present on the 8th level detail of the wavelet
389 decomposition are true detections and 14 of the 17 events present on the 6th
390 level detail of the wavelet decomposition are true detections.

391

392 5 Discussion

393 To better evaluate the number of true and false detections, we convert the
394 wavelet details into **trinary** time series. If the absolute value of the wavelet
395 detail is higher than a threshold, we replace the value by 1 (for positive values)
396 or -1 (for negative values), otherwise we replace the value by 0. We do this
397 on both the wavelet details of the GPS data and of the tremor data. Then we
398 decide that if both the GPS and the tremor time series take the value 1 (or
399 both take the value -1), we have a true detection (true positive, TP). If the
400 GPS and the tremor time series have opposite signs, or if the absolute value of
401 the GPS time series is 1 but the value of the tremor time series is 0, we have a
402 false detection (false positive, FP). If both time series take the value 0, we do
403 not have detection (true negative, TN). If the GPS time series take the value
404 0, but the absolute value of the tremor time series is 1, we miss a detection
405 (false negative, FN). We then define the sensitivity (true positive rate) and the
406 specificity (equal to 1 minus the false positive rate) as:

$$\begin{aligned} \text{sensitivity} &= \frac{TP}{TP + FN} \\ \text{specificity} &= \frac{TN}{TN + FP} \end{aligned} \tag{3}$$

407 We can then evaluate the quality of the detections obtained with our method
408 by plotting a receiver operating characteristic curve (ROC curve). The ROC
409 curve is widely use for binary classification problems in statistics and machine
410 learning. We calculate an ROC value by varying the values of the threshold
411 (here the two thresholds used to convert the GPS and the tremor time series
412 into **trinary** time series), computing the corresponding values of the true pos-
413 itive rate and the false positive rate (equal to 1 minus the specificity), and
414 plotting the true positive rate as a function of the false positive rate. If the
415 classification was made randomly, all the points would fall on the first diagonal.
416 If the classifier was perfect, the corresponding point would fall on the top left
417 corner of the graph with true positive rate equal to 1 and false positive rate equal
418 to 0. The bigger the area under the curve, the better the classification method is.

419

420 As the slow slip events are better seen on levels 6, 7 and 8 of the wavelet
421 decomposition, we first add the wavelet details corresponding to levels 6 to 8,
422 and transform the resulting time series into a **trinary** time series. We apply
423 this transform to both the GPS and the tremor time series with varying thresh-
424 olds. We then plot the ROC curve on Figure 9, each dot representing a different
425 threshold. The corresponding sums of the wavelet details for the GPS data and
426 the tremor data are shown on Figure 10. We can see that there is a trade-off
427 between sensitivity and specificity as we vary the threshold. If we decrease the
428 false positive rate, we also decrease the number of true events detected. If we
429 increase the number of true events detected, we also increase the false positive
430 rate. **If we increase the threshold for the tremor, the curve goes far-**
431 **ther away from the first diagonal, that is we get better classification**
432 **results. If we increase the threshold for the GPS, the false positive**
433 **rate and the the number of events detected decrease.** In Figure 10,

434 we have chosen thresholds for the GPS time series and the tremor time series
435 such that the specificity is higher than 0.75 (**that is the false positive rate**
436 **is lower than 0.25**), and the sensitivity is the highest possible, that is we
437 have chosen the thresholds corresponding to the dot that is farthest from the
438 diagonal, which is random.

439

440 In addition to the magnitude 6 events discussed above, Michel et al. [2019]
441 have also identified several magnitude 5 events using a variational Bayesian In-
442 dependent Component Analysis (vbICA) decomposition of the signal. As we
443 expect smaller magnitude events to be more visible at smaller time scales of
444 the wavelet decomposition (level 5), we verify for all these events whether a
445 signal can be seen at the same time as the time given in their catalog. Most
446 of these magnitude 5 events are also sub-events of bigger magnitude 6 events.
447 Table 2 summarizes for each event its timing, its number and its magnitude as
448 indicated in the catalog from Michel et al. [2019], and whether it is part of a
449 bigger magnitude 6 event. Figure 11 shows the 5th level detail wavelet decom-
450 position of the GPS data. Red lines show the timing of the big ETS events from
451 Table 1, and blue lines show the timing of the small slow slip events from Table 2.

452

453 All 14 events that are sub-events of a bigger event are visible at level 5.
454 However, this may be because the bigger events are clearly seen at levels 6 to 8,
455 and also at smaller time scales. The one small event that is not part of a bigger
456 event (Winter 2009) is visible at level 5 of the wavelet decomposition. However,
457 some other events that are not in the catalog of Michel et al. [2019]’s catalog
458 are also visible in late 2007, early 2010, early 2012, and late 2016. Therefore,
459 it is difficult to differentiate between a true detection and a false detection, and
460 to conclude whether the method can indeed detect events of magnitude 5.

461

462 In Figure 9, we see four smaller events that are not in the catalog of Michel
463 et al. [2019]: at about 2007.5, there is a negative peak followed by a positive peak
464 (that is an event in the opposite direction of what would be expected from slow
465 slip), at about 2010.2, 2012.2 and 2020.2, there are positive peaks followed by
466 negative peaks for all the sixteen locations studied in this paper. Looking back
467 at the original GPS data, there is a small increase in the displacement in the
468 eastern direction that lasts about one or two months at about 2007.5. However,
469 the direction of the displacement does not correspond to a slow slip event, and
470 another cause should be found to explain this signal. There is a decrease in
471 displacement that lasts several months at about 2010.2. This transient may
472 correspond to a long duration slow slip event. There is a small decrease in
473 displacement at about 2012.2. Its amplitude is small but the duration and
474 direction correspond to a slow slip event, so this transient could be a very small
475 slow slip event. Finally, there is also a small decrease in displacement at about
476 2020.2 that is difficult to interpret.

477 6 Conclusion

478 In this paper, we develop and test a new approach for detecting transient events
479 in GPS time series, such as slow slip events. We used wavelet methods to an-
480 alyze GNSS time series and tremor recordings of slow slip events in Cascadia.
481 We used detrended GNSS data, applied the MODWT transform, and stacked
482 the wavelet details over several nearby GNSS stations. As an independent check
483 on the timing of slow slip events, we also computed the cumulative number of
484 tremor in the vicinity of the GNSS stations, detrended this signal, and applied
485 the MODWT transform. In both time series, we could then see simultaneous
486 waveforms whose timing corresponds to the timing of slow slip events. We as-

487 sumed that there is a slow slip event whenever the wavelet signal gets above
488 a threshold. We verified that there is a good correlation between slow slip
489 events detected with only GNSS data, and slow slip events detected with only
490 tremor data. The wavelet-based detection method detects all events of magni-
491 tude higher than 6 as determined by independent event catalogs (e.g. [Michel
492 et al., 2019]). We detected signals in the GPS data that could be magnitude
493 5 events, but it is not easy to differentiate between true detections and false
494 detections.

495 Data and Resources

496 The GPS recordings used for this analysis can be downloaded from the PANGA
497 website [GPS/GNSS Network and Geodesy Laboratory: Central Washington
498 University, other/seismic network, 1996] <http://www.panga.cwu.edu/>. The
499 Python scripts used to analyze the data and make the figures can be found
500 on the first author's Github account <https://github.com/ArianeDucellier/>
501 `slowlip`. Figure 4 was created using GMT [Wessel and Smith, 1991].

502 Acknowledgements

503 This work was funded by the grant from the National Science Foundation EAR-
504 1358512. A.D. would like to thank Professor Donald Percival for introducing
505 her to wavelet methods during his excellent class on Wavelets: Data Analysis,
506 Algorithms and Theory taught at University of Washington.

507 Declaration of Competing Interests

508 The authors declare no competing interests.

509 **References**

- 510 A.C. Aguiar, T.I. Melbourne, and C.W. Scrivner. Moment release rate of Cas-
511 cadia tremor constrained by GPS. *J. Geophys. Res.*, 114:B00A05, 2009.
- 512 S. Alba, R. J. Weldon, D. Livelybrooks, and D. A. Schmidt. Cascadia ETS
513 events seen in tidal records (1980–2011). *Bull. Seismol. Soc. Am.*, 109(2):
514 812–821, 2019.
- 515 P. Audet and Y.H. Kim. Teleseismic constraints on the geological environment
516 of deep episodic slow earthquakes in subduction zone forearcs: A review.
517 *Tectonophysics*, 670:1–15, 2016.
- 518 N. M. Bartlow. A longterm view of episodic tremor and slip in Cascadia. *Geo-
519 physical Research Letters*, 43(3):e2019GL085303, 2020.
- 520 G.C. Beroza and S. Ide. Slow earthquakes and nonvolcanic tremor. *Annu. Rev.
521 Earth Planet. Sci.*, 39:271–296, 2011.
- 522 W.B. Frank. Slow slip hidden in the noise: The intermittence of tectonic release.
523 *Geophys. Res. Lett.*, 43:10125–10133, 2016.
- 524 GPS/GNSS Network and Geodesy Laboratory: Central Washington University,
525 other/seismic network. Pacific Northwest Geodetic Array (PANGA), 1996.
526 URL <http://www.panga.cwu.edu/>.
- 527 K. Hall, H. Houston, and D. Schmidt. Spatial comparisons of tremor and slow
528 slip as a constraint on fault strength in the northern Cascadia subduction
529 zone. *Geochemistry, Geophysics, Geosystems*, 19(8):2706–2718, 2018.
- 530 J. C. Hawthorne and A. M. Rubin. Shorttime scale correlation between slow
531 slip and tremor in Cascadia. *Journal of Geophysical Research: Solid Earth*,
532 118:1316–1329, 2013.

- 533 Y. Hiramatsu, T. Watanabe, and K. Obara. Deep lowfrequency tremors as a
534 proxy for slip monitoring at plate interface. *Geophysical Research Letters*, 35:
535 L13304, 2008.
- 536 Y. Jiang, S. Wdowinski, T. H. Dixon, M. Hackl, M. Protti, and V. Gonzalez.
537 Slow slip events in Costa Rica detected by continuous GPS observations,
538 2002–2011. *Geochemistry, Geophysics, Geosystems*, 13:Q04006, 2012.
- 539 P. Kumar and E. Foufoula-Georgiou. Wavelet analysis for geophysical applica-
540 tions. *Rev. Geophys.*, 35(4):385–412, 1997.
- 541 S. Li, J. Freymueller, and R. McCaffrey. Slow slip events and timedependent
542 variations in locking beneath Lower Cook Inlet of the AlaskaAleutian sub-
543 duction zone. *Journal of Geophysical Research: Solid Earth*, 121:1060–1079,
544 2016.
- 545 S. Michel, A. Gualandi, and J.-P. Avouac. Interseismic coupling and slow slip
546 events on the Cascadia megathrust. *Pure Appl. Geophys.*, 176:3867–3891,
547 2019.
- 548 T. Nishimura, T. Matsuzawa, and K. Obara. Detection of shortterm slow slip
549 events along the Nankai Trough, southwest Japan, using GNSS data. *Journal*
550 *of Geophysical Research: Solid Earth*, 118:3112–3125, 2013.
- 551 K. Obara. Nonvolcanic deep tremor associated with subduction in southwest
552 Japan. *Science*, 296(5573):1679–1681, 2002.
- 553 R. Ohtani, J.J. McGuire, and P. Segall. Network strain filter: A new tool for
554 monitoring and detecting transient deformation signals in GPS arrays. *J.*
555 *Geophys. Res.*, 115:B12418, 2010.
- 556 D.B. Percival and A.T. Walden. *Wavelet Methods for Time Series Analysis*.

- 557 Cambridge Series in Statistical and Probabilistic Mathematics. Cambridge
558 University Press, New York, NY, USA, 2000.
- 559 L.A. Preston, K.C. Creager, R.S. Crosson, T.M. Brocher, and A.M. Trehu.
560 Intraslab earthquakes: Dehydration of the Cascadia slab. *Science*, 302:1197–
561 1200, 2003.
- 562 M. Radiguet, F. Cotton, M. Vergnolle, M. Campillo, A. Walpersdorf, N. Cotte,
563 and V. Kostoglodov. Slow slip events and strain accumulation in the Guerrero
564 gap, Mexico. *Journal of Geophysical Research: Solid Earth*, 117:B04305, 2012.
- 565 G. Rogers and H. Dragert. Tremor and slip on the Cascadia subduction zone:
566 The chatter of silent slip. *Science*, 300(5627):1942–1943, 2003.
- 567 D. A. Schmidt and H. Gao. Source parameters and timedeependent slip distribu-
568 tions of slow slip events on the Cascadia subduction zone from 1998 to 2008.
569 *Journal of Geophysical Research: Solid Earth*, 115:B00A18, 2010.
- 570 D.R. Shelly, G.C. Beroza, and S. Ide. Non-volcanic tremor and low-frequency
571 earthquake swarms. *Nature*, 446:305–307, 2007.
- 572 W. Szeliga, T.I. Melbourne, M.M. Miller, and V.M. Santillan. Southern Casca-
573 dia episodic slow earthquakes. *Geophys. Res. Lett.*, 31:L16602, 2004.
- 574 W. Szeliga, T. Melbourne, M. Santillan, and M. Miller. GPS constraints on 34
575 slow slip events within the Cascadia subduction zone, 1997-2005. *J. Geophys.*
576 *Res.*, 113:B04404, 2008.
- 577 E.K. Todd and S.Y. Schwartz. Tectonic tremor along the northern Hikurangi
578 Margin, New Zealand, between 2010 and 2015. *J. Geophys. Res. Solid Earth*,
579 121:8706–8719, 2016.
- 580 M. Vergnolle, A. Walpersdorf, V. Kostoglodov, P. Tregoning, J. A. Santiago,
581 N. Cotte, and S. I. Franco. Slow slip events in Mexico revised from the

- 582 processing of 11 year GPS observations. *Journal of Geophysical Research: Solid Earth*, 115:B08403, 2010.
- 584 L. M. Wallace. Slow slip events in New Zealand. *Annual Review of Earth and Planetary Sciences*, 48:175–203, 2020.
- 586 L. M. Wallace, J. Beavan, S. Bannister, and C. Williams. Simultaneous longterm
587 and shortterm slow slip events at the Hikurangi subduction margin, New
588 Zealand: Implications for processes that control slow slip event occurrence,
589 duration, and migration. *Journal of Geophysical Research: Solid Earth*, 117:
590 B11402, 2012.
- 591 A.G. Wech. Interactive tremor monitoring. *Seismol. Res. Lett.*, 81(4):664–669,
592 2010.
- 593 A.G. Wech. Extending Alaska’s plate boundary; tectonic tremor generated by
594 Yakutat subduction. *Geology*, 44(7):587–590, 2016.
- 595 M. Wei, J.J. McGuire, and E. Richardson. A slow slip event in the south central
596 Alaska Subduction Zone. *Geophys. Res. Lett.*, 39:L15309, 2012.
- 597 P. Wessel and W. H. F. Smith. Free software helps map and display data. *EOS Trans. AGU*, 72:441, 1991.

⁵⁹⁹ **Addresses**

⁶⁰⁰ Ariane Ducellier. University of Washington, Department of Earth and Space
⁶⁰¹ Sciences, Box 351310, 4000 15th Avenue NE Seattle, WA 98195-1310.

⁶⁰²

⁶⁰³ Kenneth C. Creager. University of Washington, Department of Earth and
⁶⁰⁴ Space Sciences, Box 351310, 4000 15th Avenue NE Seattle, WA 98195-1310.

⁶⁰⁵

⁶⁰⁶ David A. Schmidt. University of Washington, Department of Earth and
⁶⁰⁷ Space Sciences, Box 351310, 4000 15th Avenue NE Seattle, WA 98195-1310.

Tables

Table 1: Episodic Tremor and Slip events with $M \geq 6$ identified by MODWT in both the GPS and the tremor data. The duration and the number of tremor are from the tremor catalog of the PNSN. The event number and the magnitude are from the slow slip catalog of Michel et al. [2019].

Time	Duration (days)	Number of tremor (hours)	Event number	Magnitude
2007.06	28	398	3	6.68
2008.36	25	402	10	6.56
2009.35	24	248	16	6.49
2010.63	29	518	24	6.54
2011.60	37	479	30	6.47
2012.72	37	620	34	6.54
2013.71	27	423	41	6.58
2014.65	15	190	48	6.03
2014.89	38	385	51	6.40
2016.11	43	421	54	6.79
2017.23	19	279	59	6.61
2018.49	22	381		
2019.23	34	195		
2019.88	16	205		
2020.79	26	193		
2020.86	12	162		
2021.09	14	230		

Table 2: Magnitude 5 events from Michel et al. [2019].

Time	Event number	Magnitude	Sub-event of bigger event
2007.06	1	5.64	Yes
2007.08	2	5.91	Yes
2008.38	11	5.50	Yes
2009.16	14	5.50	No
2009.36	17	5.32	Yes
2010.63	25	5.76	Yes
2011.66	31	5.61	Yes
2011.66	32	5.32	Yes
2012.69	35	5.56	Yes
2013.74	42	5.71	Yes
2014.69	49	5.31	Yes
2014.93	52	5.39	Yes
2016.03	57	5.80	Yes
2017.13	60	5.43	Yes
2017.22	61	5.37	Yes

609 **Figure captions**

- 610 • Figure 1. Demonstration of a wavelet decomposition for a synthetic dataset.
- 611 A synthetic time series is created (top row) with steps of period 500 days,
- 612 and transient durations of 2 days (left), 5 days, 10 days, and 20 days
- 613 (right). The resulting details and smooths are shown in increasing level.
- 614 The amplitude of the synthetic time series is normalized to 1, and the
- 615 details and smooths show the relative amplitude.
- 616 • Figure 2. Top: **Original data from GPS station PGC5 (black)**
- 617 and same data where displacement values have been artificially
- 618 removed at two different times (**2010.97 on the left and 2011.48**
- 619 on the right) and replaced by the sum of a straight line and
- 620 a Gaussian noise component (red). The corresponding ten details
- 621 and smooths of the wavelet composition are shown in increasing levels for
- 622 the original data (black) and for the **data with displacement values**
- 623 **removed and replaced** by linear interpolation plus Gaussian noise (red).
- 624 • Figure 3. Top: Longitudinal displacement recorded at GPS station PGC5.
- 625 The resulting details and smooth of the wavelet decomposition are shown
- 626 in increasing level.
- 627 • Figure 4. GPS stations used in this study (black triangles). The black
- 628 line represents the 40 km depth contour of the plate boundary model by
- 629 Preston et al. [2003]. The red triangles are the locations where we stack
- 630 the GPS data. The small grey dots are all the tremor locations from the
- 631 PNSN catalog.
- 632 • Figure 5. Details and smooth of the wavelet decomposition of the de-
- 633 trended cumulative tremor count around the third northernmost red tri-
- 634 angles on Figure 3 (latitude 48.5).

- Figure 6. Top: Stacked 8th level details of the wavelet decomposition of the displacement over all the GPS stations located in a 50 km radius of a given point, for the 16 red triangles indicated in Figure 3. Bottom: 8th level detail multiplied by -1 of the cumulative tremor count in a 50 km radius of a given point for the same 16 locations. The black lines represent the timings of the ETS events from Table 1. We mark by a red rectangle every time where the amplitude is higher than a threshold of 0.4 (for the GPS) or 0.003 (for the tremor). We mark by a blue rectangle every time where the amplitude is lower than minus the threshold.
- Figure 7. Same as Figure 6 but for the 7th level detail. The thresholds are 0.5 (for the GPS) and 0.01 (for the tremor).
- Figure 8. Same as Figure 6 but for the 6th level detail. The thresholds are 0.3 (for the GPS) and 0.009 (for the tremor).
- Figure 9. ROC curve for the sum of the 6th, 7th, and 8th level details of the wavelet decomposition. Each dot represents the true positive rate of event detections and the false positive rate of event detections for a given pair of thresholds (for the GPS and for the tremor). The **black** cross marks the true positive rate and the false positive rate obtained with the thresholds used to make Figure 10. **The values of the threshold are color-coded. Reds correspond to the lowest value of the threshold for the tremor (0.001), while oranges, greens, blues, purples correspond to increasing values of the threshold for the tremor (up to 0.01). The brightest colors correspond to the highest values of the threshold for the GPS (1.5), while the darker and darker colors correspond to decreasing values of the threshold for the GPS (0.1).**

- 661 • Figure 10. Same as Figure 6 but for the sum of the 6th, 7th and 8th level
662 details. The thresholds are 0.8 (for the GPS) and 0.01 (for the tremor).
- 663 • Figure 11. Top: Stacked 5th level details of the wavelet decomposition
664 of the displacement over all the GPS stations located in a 50 km radius
665 of a given point, for the 16 red triangles indicated in Figure 3. The red
666 lines represent the timings of the ETS events from Table 1. The blue
667 lines represent the timings of the magnitude 5 events from the catalog of
668 Michel et al. [2019].

₆₆₉ **Figures**

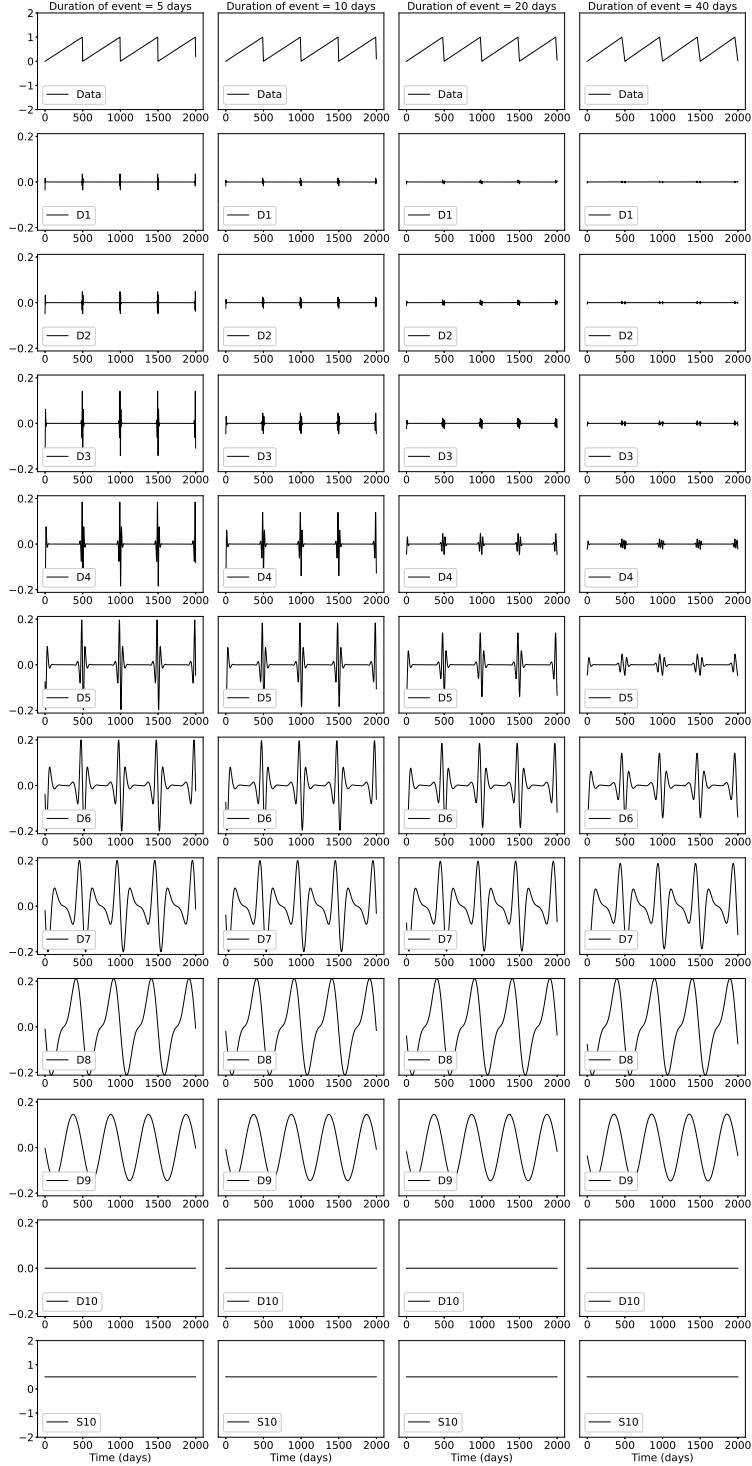


Figure 1: Demonstration of a wavelet decomposition for a synthetic dataset. A synthetic time series is created (top row) with steps of period 500 days, and transient durations of 2 days (left), 5 days, 10 days, and 20 days (right). The resulting details and smooths are shown in increasing level. The amplitude of the synthetic time series is normalized to 1, and the details and smooths show the relative amplitude.

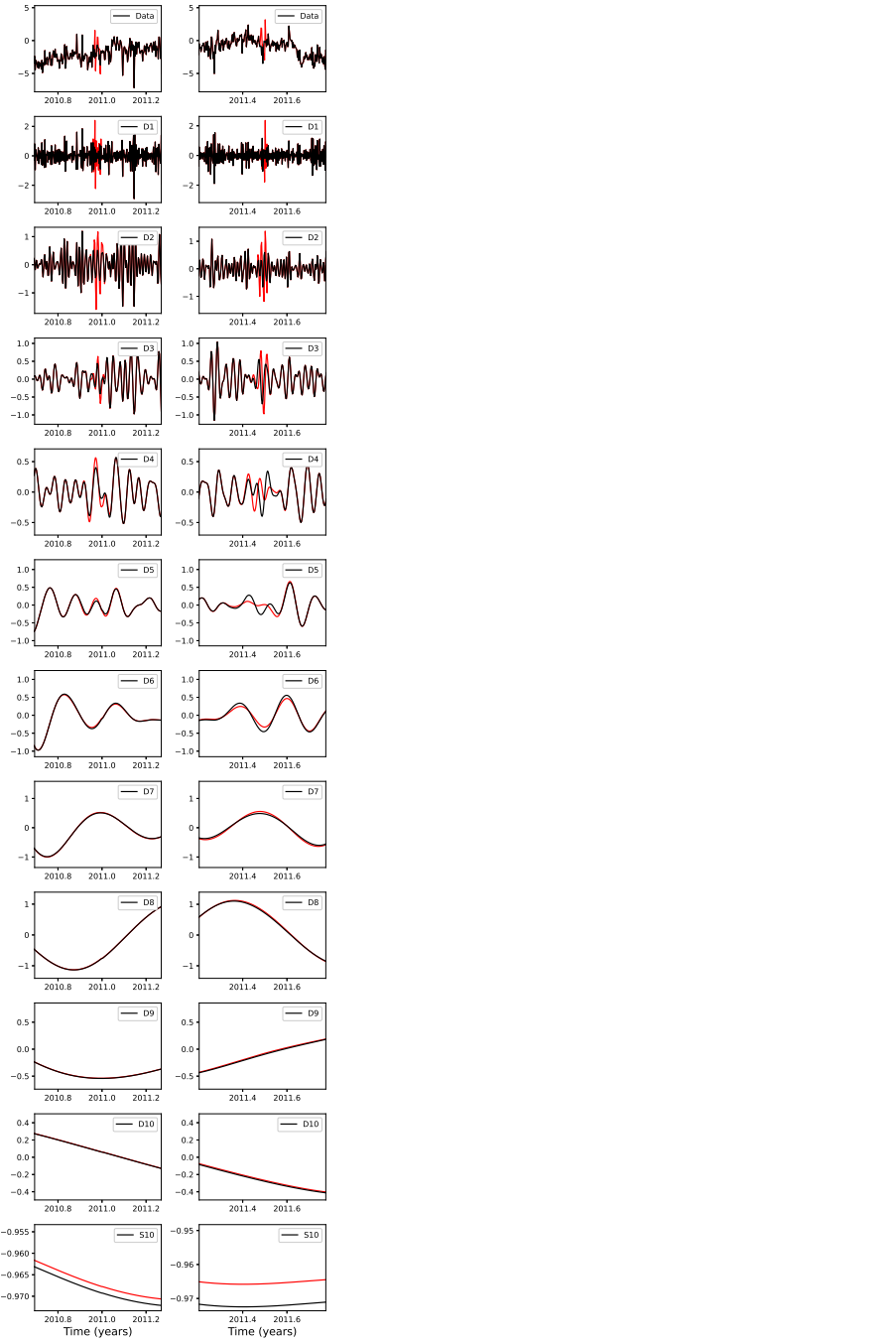


Figure 2: Top: Original data from GPS station PGC5 (black) and same data where displacement values have been artificially removed at two different times (2010.97 on the left and 2011.48 on the right) and replaced by the sum of a straight line and a Gaussian noise component (red). The corresponding ten details and smooths of the wavelet composition are shown in increasing levels for the original data (black) and for the data with displacement values removed and replaced by linear interpolation plus Gaussian noise (red).

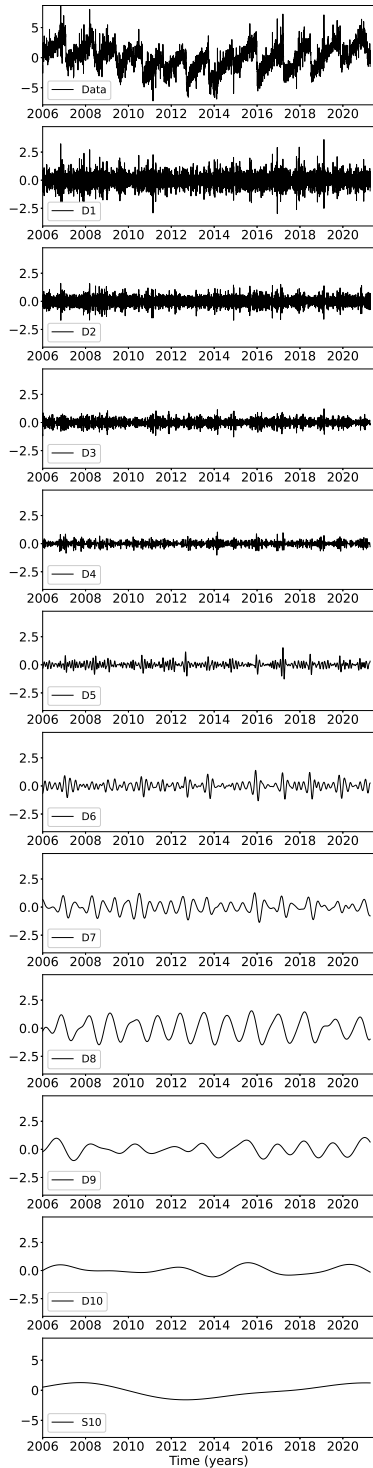


Figure 3: Top: Longitudinal displacement recorded at GPS station PGC5. The resulting details and smooth of the wavelet decomposition are shown in increasing level.

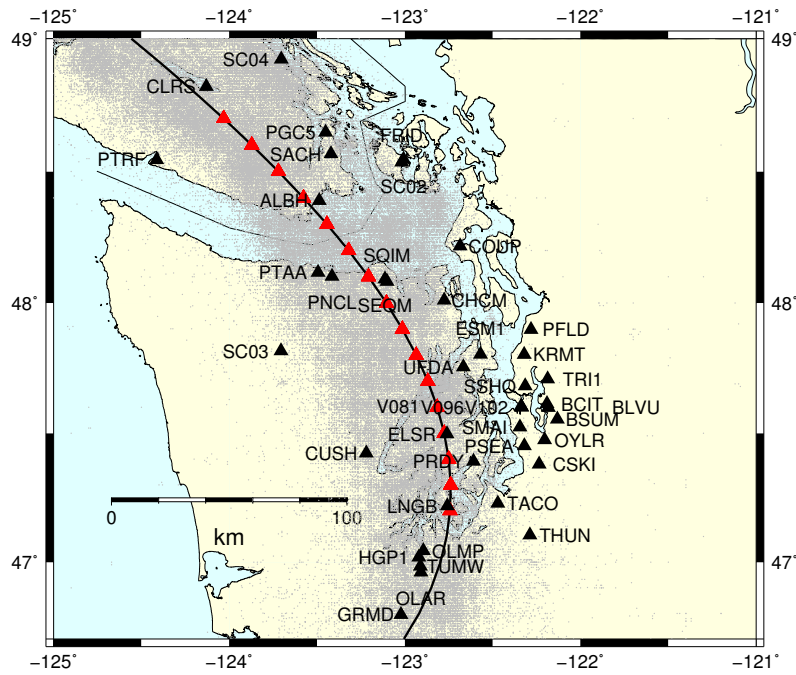


Figure 4: GPS stations used in this study (black triangles). The black line represents the 40 km depth contour of the plate boundary model by Preston et al. [2003]. The red triangles are the locations where we stack the GPS data. The small grey dots are all the tremor locations from the PNSN catalog.

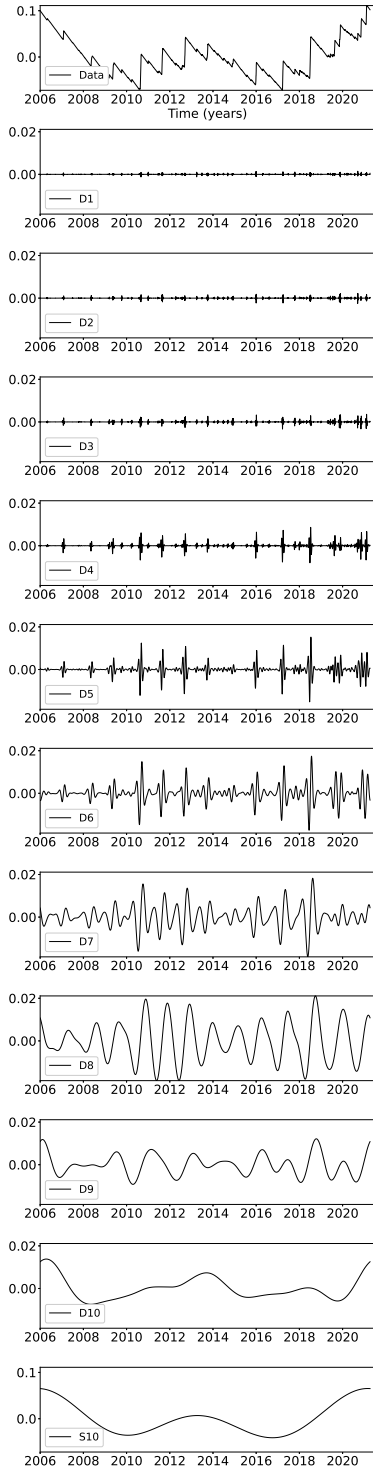


Figure 5: Details and smooth of the ³³wavelet decomposition of the detrended cumulative tremor count around the third northernmost red triangles on Figure 3 (latitude 48.5).

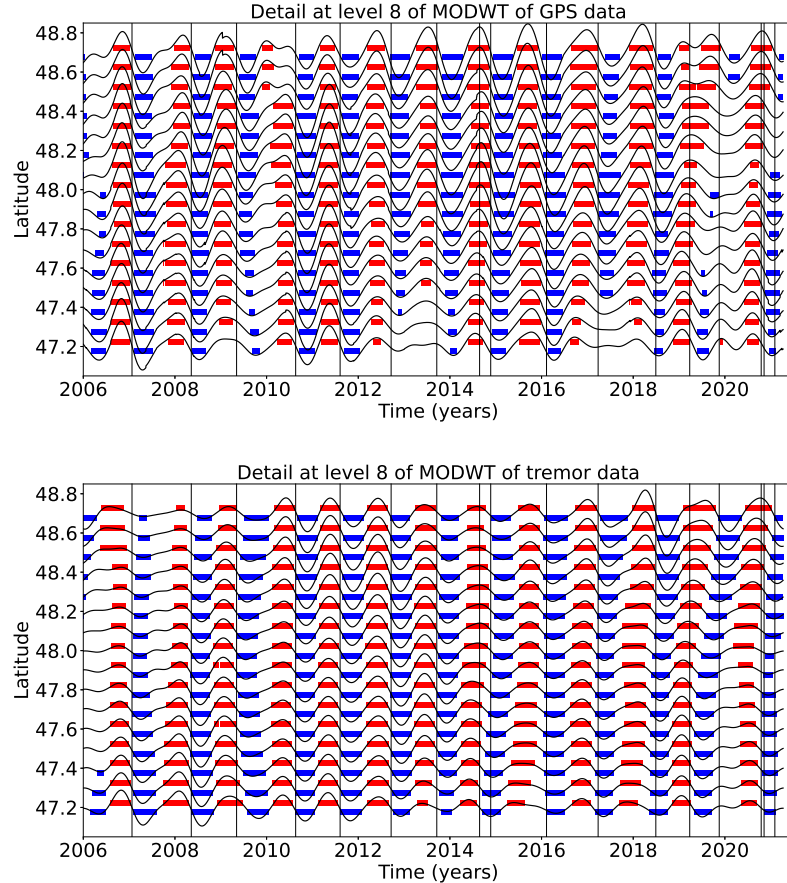


Figure 6: Top: Stacked 8th level details of the wavelet decomposition of the displacement over all the GPS stations located in a 50 km radius of a given point, for the 16 red triangles indicated in Figure 3. Bottom: 8th level detail multiplied by -1 of the cumulative tremor count in a 50 km radius of a given point for the same 16 locations. The black lines represent the timings of the ETS events from Table 1. We mark by a red rectangle every time where the amplitude is higher than a threshold of 0.4 (for the GPS) or 0.003 (for the tremor). We mark by a blue rectangle every time where the amplitude is lower than minus the threshold.

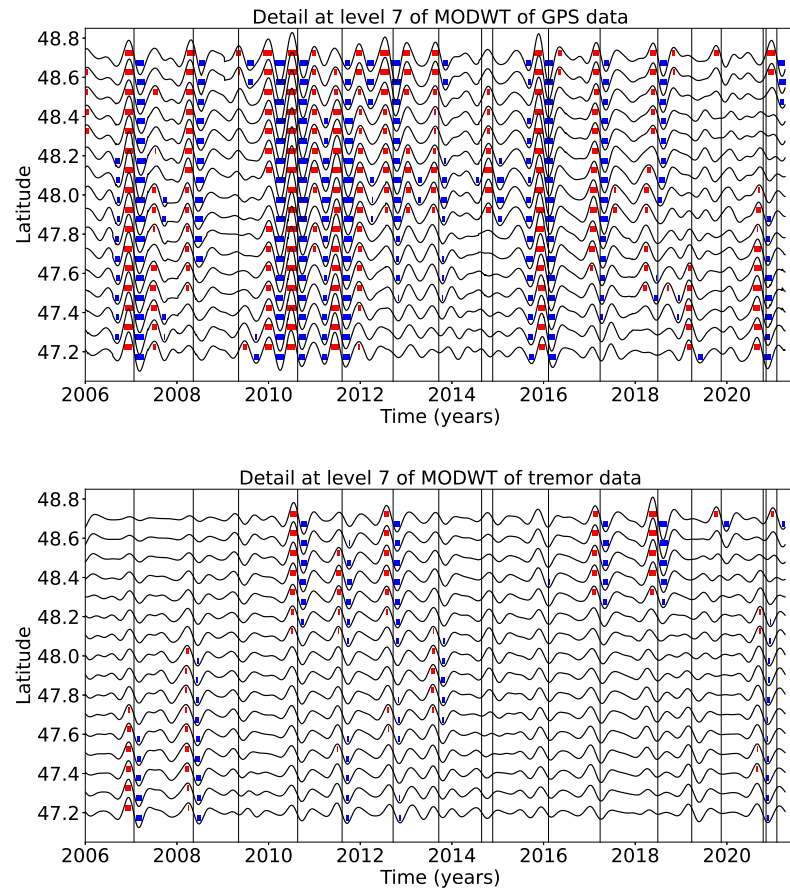


Figure 7: Same as Figure 6 but for the 7th level detail. The thresholds are 0.5 (for the GPS) and 0.01 (for the tremor).

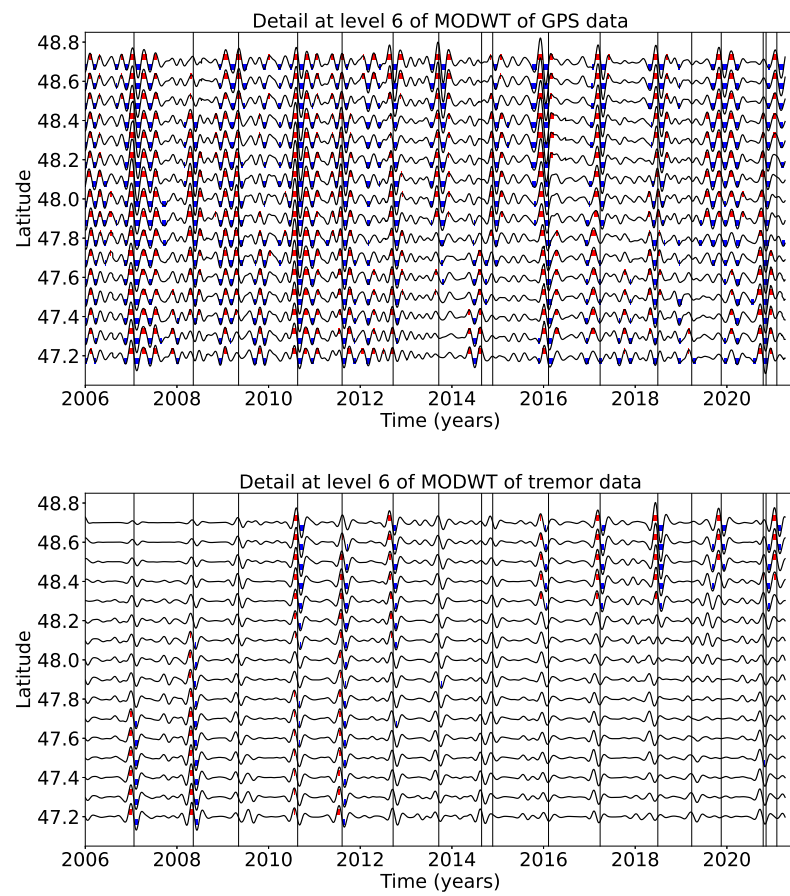


Figure 8: Same as Figure 6 but for the 6th level detail. The thresholds are 0.3 (for the GPS) and 0.009 (for the tremor).

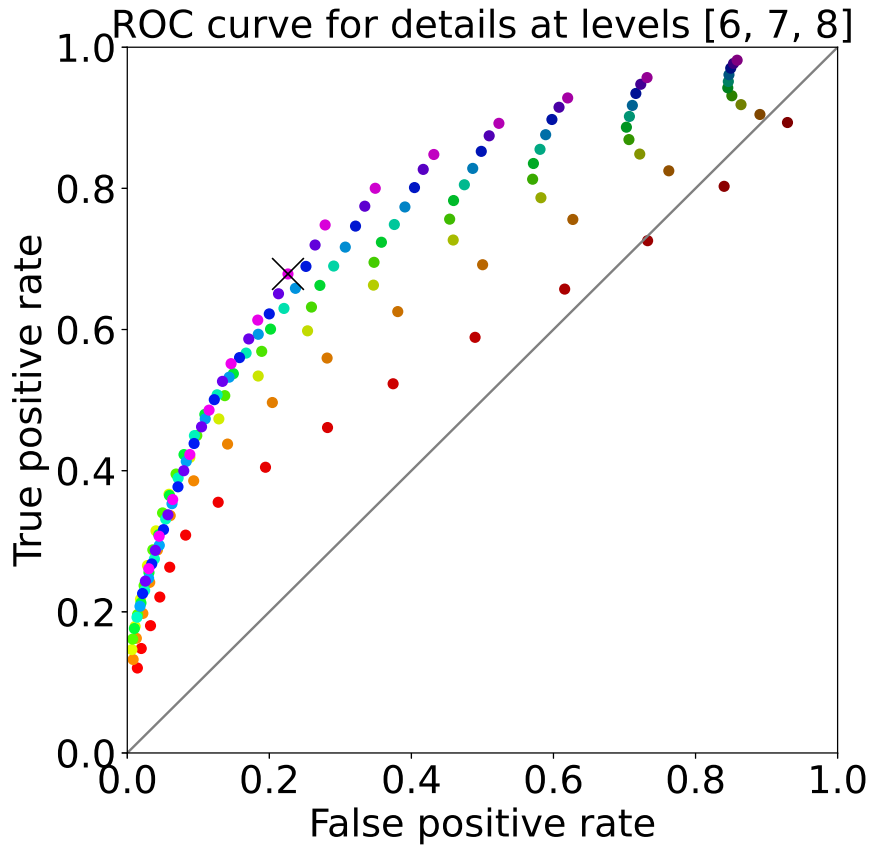


Figure 9: ROC curve for the sum of the 6th, 7th, and 8th level details of the wavelet decomposition. Each dot represents the true positive rate of event detections and the false positive rate of event detections for a given pair of thresholds (for the GPS and for the tremor). The **black** cross marks the true positive rate and the false positive rate obtained with the thresholds used to make Figure 10. **The values of the threshold are color-coded.** Reds correspond to the lowest value of the threshold for the tremor (0.001), while oranges, greens, blues, purples correspond to increasing values of the threshold for the tremor (up to 0.01). The brightest colors correspond to the highest values of the threshold for the GPS (1.5), while the darker and darker colors correspond to decreasing values of the threshold for the GPS (0.1).

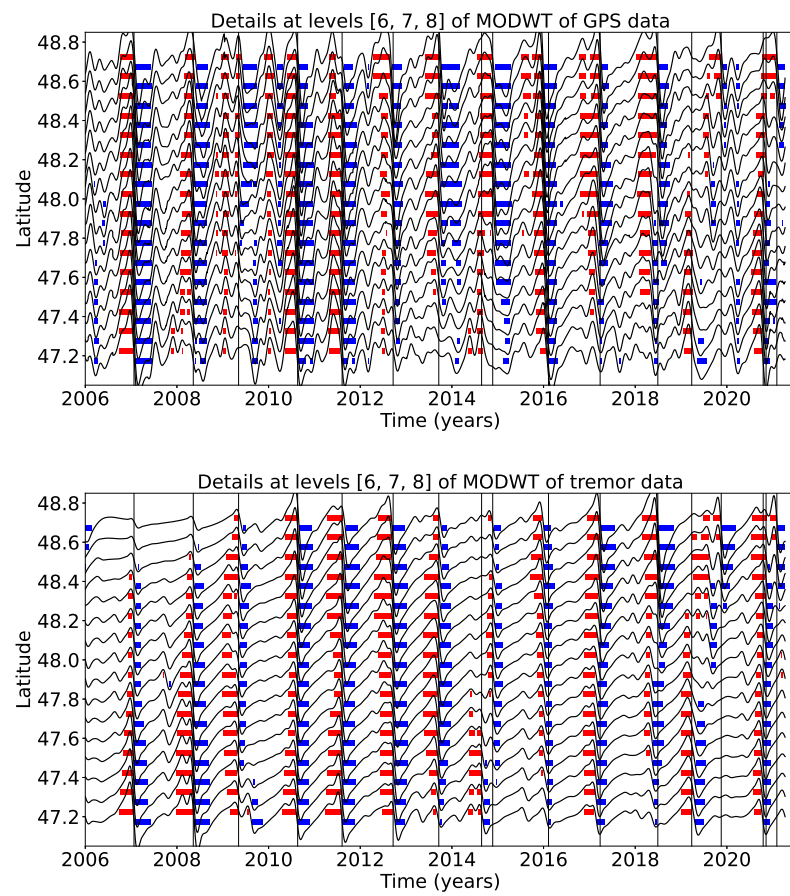


Figure 10: Same as Figure 6 but for the sum of the 6th, 7th and 8th level details. The thresholds are 0.8 (for the GPS) and 0.01 (for the tremor).

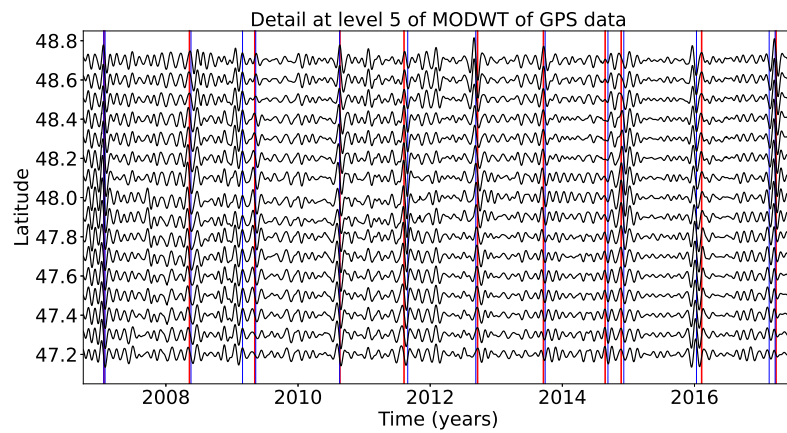


Figure 11: Top: Stacked 5th level details of the wavelet decomposition of the displacement over all the GPS stations located in a 50 km radius of a given point, for the 16 red triangles indicated in Figure 3. The red lines represent the timings of the ETS events from Table 1. The blue lines represent the timings of the magnitude 5 events from the catalog of Michel et al. [2019].